

# Deeper-PINNs: Element-wise Multiplication Based Physics-informed Neural Networks

Feilong Jiang<sup>a</sup>      Xiaonan Hou<sup>a\*</sup>      Min Xia<sup>b\*</sup>

<sup>a</sup> Department of Engineering, Lancaster University, LA1 4YW Lancaster, U.K.

<sup>b</sup> Department of Mechanical and Materials Engineering, University of Western Ontario, London, Ontario, Canada

x.hou2@lancaster.ac.uk

mxia47@uwo.ca

## Abstract

As a promising framework for resolving partial differential equations (PDEs), physics-informed neural networks (PINNs) have received widespread attention from industrial and scientific fields. However, lack of expressive ability and initialization pathology issues are found to prevent the application of PINNs in complex PDEs. In this work, we propose Deeper Physics-Informed Neural Network (Deeper-PINN) to resolve these issues. The element-wise multiplication operation is adopted to transform features into high-dimensional, non-linear spaces. Benefiting from element-wise multiplication operation, Deeper-PINNs can alleviate the initialization pathologies of PINNs and enhance the expressive capability of PINNs. The proposed structure is verified on various benchmarks. The results show that Deeper-PINNs can effectively resolve the initialization pathology and exhibit strong expressive ability.

## 1. Introduction

As an important role in scientific machine learning field, physics-informed neural networks (PINNs) appear to be a promising method for resolving partial differential equations (PDEs) [1]. Utilizing the physical laws as the constraints of neural networks, PINNs show better interpretability and generalization ability than traditional data-driven machine learning models. As an alternative of traditional numerical algorithms, PINNs have been widely applied in scientific and engineering fields [2-5].

Although promising outcomes have been presented, PINNs have been observed of failing resolving some PDEs, especially when the solutions exhibit high-frequency or multi-scale characteristics [6], [7]. Many efforts have been made to improve the capability of PINNs. To resolve the loss terms unbalancing problem, methods such as NTK-based weighting [6], Grad Norm [8] and SoftAdapt [9] are used to weight different loss term for training PINNs effectively. Utilizing the geometry-aware approximations [10] or Fourier feature embedding [11] methods, the boundary conditions can be exactly imposed during the training process. Consequently, the accuracy of PINNs can be effectively improved. Since the training process of PINNs may go against physical casualty, training methods that follow the spatio-temporal causal are proposed to improve the accuracy of PINNs [12-14]. The loss imbalance problem between different training points prevents PINNs from resolving PDEs correctly. This issue can be resolved by introducing adaptive weighting scheme [15-18] or adaptive resampling method [19], [20]. New neural network structures such as mMLP [8], Fourier feature embedding [7], DM-PINNs [21] and SPINN [22] are also proven to be useful for improving the representative capability of PINNs.

Despite the success of these research, most existing works still use small neural networks with a few layers, which limits the capability of PINNs. This is attributed to the gradient vanishing issue of deep PINNs structure, which limits the representative capability of PINNs. Recent research has proved that the initialization pathologies [23] of PINNs can intensify

vanishing gradient. To overcome this limitation, we propose a novel architecture which is Deeper-PINNs. By doing element-wise multiplication between 2 sub-layers, the outputs of the 2 layers are fused together and projected into nonlinear-high-dimensional feature spaces. In this way the initialization pathologies can be eliminated, and expressive ability of PINNs can be effectively improved. Besides, with the stacking of a series of shortcut connected multiplication blocks, the model can use deeper neural network structure and obtain better results.

## 2. Related works

### Physics-informed Neural Networks (PINNs)

Following the original work of physics-informed neural networks (PINNs) as outlined in [1], the typical form of partial differential equation (PDEs) can be represented as:

$$u_t + \mathcal{N}[u] = 0, \quad t \in [0, T], \quad x \in \Omega, \quad (1)$$

where  $u$  indicates the latent solution,  $\mathcal{N}[\cdot]$  represents a linear or nonlinear differential operator. The initial and boundary conditions are in the forms of:

$$u(0, x) = g(x), \quad x \in \Omega, \quad (2)$$

$$\mathcal{B}[u] = 0, \quad t \in [0, T], \quad x \in \partial\Omega, \quad (3)$$

where  $g(x)$  is a given function,  $\mathcal{B}[\cdot]$  indicates boundary operator.

The core idea of PINNs is approximating the latent solution  $u(t, x)$  with a neural network  $u_\theta(t, x)$ , where  $\theta$  represents trainable parameters of the neural network (NN). Instead of utilizing the difference between label data  $u(t, x)$  and the prediction of NN  $u_\theta(t, x)$ , PINNs directly utilizes the PDE and the corresponding initial and boundary conditions as the loss function. Utilizing automatic differentiation [24], the required gradients with respect to input variables can be obtained. The loss function can be expressed as:

$$\mathcal{L}(\theta) = \lambda_{ic} \mathcal{L}_{ic}(\theta) + \lambda_{bc} \mathcal{L}_{bc}(\theta) + \lambda_r \mathcal{L}_r(\theta), \quad (4)$$

where

$$\mathcal{L}_{ic}(\theta) = \frac{1}{N_{ic}} \sum_{i=1}^{N_{ic}} |u_\theta(0, x_{ic}^i) - g(x_{ic}^i)|^2, \quad (5)$$

$$\mathcal{L}_{bc}(\theta) = \frac{1}{N_{bc}} \sum_{i=1}^{N_{bc}} |\mathcal{B}[u_\theta](t_{bc}^i, x_{bc}^i)|^2, \quad (6)$$

$$\mathcal{L}_r(\theta) = \frac{1}{N_r} \sum_{i=1}^{N_r} \left| \frac{\partial u_\theta}{\partial t}(x_r^i, t_r^i) + \mathcal{N}[u_\theta](x_r^i, t_r^i) \right|^2, \quad (7)$$

$\lambda$  represents the weighting coefficient, which is used to balance different loss terms [25].

Under these conditions, the training procedure of PINNs can be interpreted as solving the given PDEs without any labelled data.

### Tackling initialization pathologies of PINNs

For PINNs, the derivative operations of the output  $u_\theta$  is implemented before the backpropagation. As proven by Wang et al. [23], such operations will reduce the nonlinear expressively ability of PINNs at the initialization state especially when the number of layers increases. Consequently, the initialization pathologies of PINNs intensifies vanishing gradient. To alleviate such problem, Wang et al. proposed the PirateNet structure [23]. With the residual adaptive operations, the model will be initialized as a single layer neural network. Thus, the initialization pathology induced by the increasing of the depth. Different from the PirateNet, we aim to tackle the initialization pathology by constructing a new neural network

structure, which enables PINNs with strong nonlinear expressive ability even after the derivative operations.

### 3. Deeper-PINNs

The structure of Deeper-PINN is shown in Figure 1. The basic layer of Deeper-PINN is element-wise multiplied layer (EM-layer), which contains  $k$  ( $k > 1$ ) sublayers. The inputs  $\mathbf{x}$  are fed into  $k$  fully connected layers with the same width. The outputs of the  $k$  layers are then element-wise multiplied and get a non-linear high-dimensional output  $\mathbf{H}^{(1)}$ :

$$\mathbf{H}^{(1)} = \sigma(\mathbf{W}_1 \cdot \mathbf{x} + \mathbf{b}_1) \odot \sigma(\mathbf{W}_2 \cdot \mathbf{x} + \mathbf{b}_2) \odot \cdots \odot \sigma(\mathbf{W}_k \cdot \mathbf{x} + \mathbf{b}_k), \quad (8)$$

where  $\sigma$  denotes activation function,  $\mathbf{W}$  represents weights,  $\mathbf{b}$  represents biases.  $\mathbf{H}^{(1)}$  is then input into  $N$  shortcut connection blocks. Each shortcut connection block contains 2 element-wise multiplication layers. With  $\mathbf{H}^{(l)}$  as the input of  $l$ -th block ( $1 \leq l \leq N$ ), the forward process of each shortcut connection block can be expressed as:

$$\mathbf{h}_1^{(l)} = \sigma(\mathbf{W}_{11}^{(l)} \cdot \mathbf{H}^{(l)} + \mathbf{b}_{11}^{(l)}) \odot \sigma(\mathbf{W}_{12}^{(l)} \cdot \mathbf{H}^{(l)} + \mathbf{b}_{12}^{(l)}) \odot \cdots \odot \sigma(\mathbf{W}_{1k}^{(l)} \cdot \mathbf{H}^{(l)} + \mathbf{b}_{1k}^{(l)}), \quad (9)$$

$$\mathbf{h}_2^{(l)} = \sigma(\mathbf{W}_{21}^{(l)} \cdot \mathbf{h}_1^{(l)} + \mathbf{b}_{21}^{(l)}) \odot \sigma(\mathbf{W}_{22}^{(l)} \cdot \mathbf{h}_1^{(l)} + \mathbf{b}_{22}^{(l)}) \odot \cdots \odot \sigma(\mathbf{W}_{2k}^{(l)} \cdot \mathbf{h}_1^{(l)} + \mathbf{b}_{2k}^{(l)}), \quad (10)$$

$$\mathbf{H}^{(l+1)} = \mathbf{h}_2^{(l)} + \mathbf{H}^{(l)}, \quad (11)$$

the final output  $u_\theta$  is given by:

$$u_\theta = \mathbf{H}^{(N)} \cdot \mathbf{W}^{(N+1)} + \mathbf{b}^{(N+1)}. \quad (12)$$

Notice that the first layer of Deeper-PINN is responsible for transforming the dimension of inputs. It can also be replaced by other structures such as a dense layer or random Fourier features.

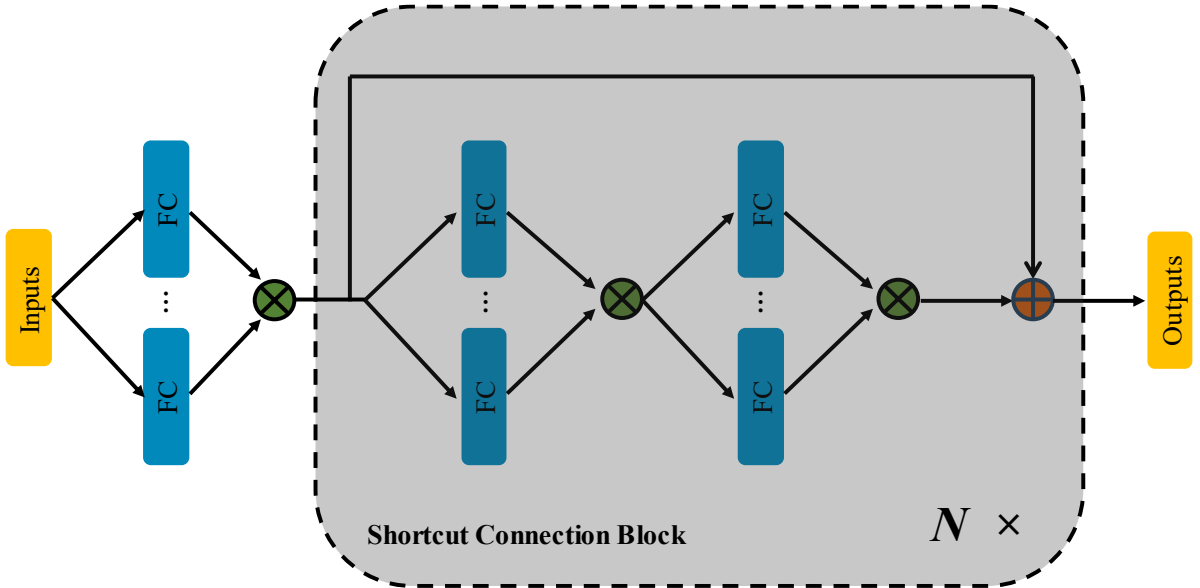


Figure 1: The structure of Deeper-PINNs.

In [23], Wang et al. verified the traditional MLP can suffer from the initialization pathology, which makes  $\frac{\partial u_\theta}{\partial x}$  perform as a linear network. Under such circumstance, the model will be

hard to approximate the solution derivatives. For our method, however, the element-wise multiplication can still project the features from different subnet into a nonlinear space, which prevent the initialization pathology. The proof is shown below:

Consider the proposed structure without shortcut connections. With the input as  $x$ , the output  $u_\theta(x)$  can be expressed as follows:

$$u_\theta^{(l)}(x) = g_1^l \odot g_2^l \odot \cdots \odot g_k^l, \quad g_i^l = \sigma(\mathbf{W}_i^{(l)} u_\theta^{(l-1)}(x) + \mathbf{b}_i^{(l)}), \quad l=1,2,\dots,L, \quad i=1,2,\dots,k, \quad (13)$$

$L$  represents the number of hidden layers,  $u_\theta^{(0)}(x) = x$ . Assuming that the neural network operates within a linear regime. Under such circumstance,  $\sigma(x) \approx x$ . When all biases are initialized as 0, the output of the final layer is:

$$u_\theta(x) \approx \prod_{i=1}^L \left( (\mathbf{W}_1^i \odot \mathbf{W}_2^i \odot \dots \odot \mathbf{W}_k^i)^{L-i+1} \right) \cdot \mathbf{W}^{(L+1)} \cdot x^{k^L}. \quad (14)$$

The first-order derivate of  $u_\theta(x)$  will be:

$$\frac{\partial u_\theta}{\partial x}(x) \approx k^L \cdot \prod_{i=1}^L \left( (\mathbf{W}_1^i \odot \mathbf{W}_2^i \odot \dots \odot \mathbf{W}_k^i)^{L-i+1} \right) \cdot \mathbf{W}^{(L+1)} \cdot x^{k^L-1}. \quad (15)$$

For MLP, as give in [23], the first-order derivate of  $u_\theta(x)$  under such assumption is:

$$\frac{\partial u_\theta}{\partial x}(x) \approx \mathbf{W}^{(L+1)} \cdot \mathbf{W}^{(L)} \dots \mathbf{W}^{(1)}. \quad (16)$$

Apparently, the MLP degrades as a deep linear network at initialization when calculating  $\frac{\partial u_\theta}{\partial x}$ . However, owing to the element-wise multiplication, our method still has nonlinear expressive ability.

To demonstrate the effectiveness of our method, we empirically validate our model on 1D advection equation which can be expressed as:

$$\frac{\partial u}{\partial t} + \beta \frac{\partial u}{\partial x} = 0, \quad x \in [0, 2\pi], \quad t \in [0, 1], \quad (17)$$

$$u(0, x) = \sin(x), \quad (18)$$

$$u(t, 0) = u(t, 2\pi), \quad (19)$$

where we set  $\beta$  as 100, which has been commonly used for PINNs. For Deeper-PINN, each layer contains 2 sublayers. The models are trained with Adam optimizer for 50,000 iterations with an initial learning rate of 0.001, and an exponential decay rate of 0.9 every 1000 iterations. All the outcomes are averaged from 5 independent trials.

Figure 2 shows the  $L^2$  error of ResNet [26] and the proposed method in different depth. It can be observed that when the depth of the neural network becomes larger, the performance of ResNet shows a degradation. However, benefiting from the element-wise multiplication operations, Deeper-PINN can obtain better results with the depth increasing.

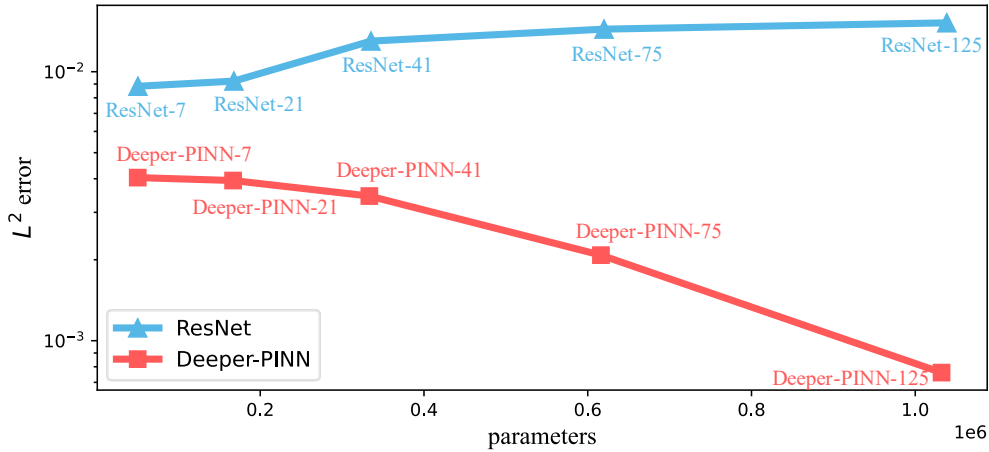


Figure 2:  $L^2$  error of ResNet and Deeper-PINN in different depth.

## 4. Experiments

### Experimental setups

For all the cases, the weights are initialized with Xavier normal distribution [27], and tanh is used as the activation function. All the training points are resampled at every iteration to

prevent the overfitting problem. Adam is utilised as the optimizer. The training is conducted on a single NVIDIA GeForce RTX 4090 GPU. All the results are averaged from 5 independent trials.

## Results

### Advection equation

We consider the 1D advection equation which is expressed as:

$$\frac{\partial u}{\partial t} + \beta \frac{\partial u}{\partial x} = 0, \quad (x, t) \in [0, 2\pi] \times [0, 1], \quad (20)$$

$$u(0, x) = \sin(x), \quad (21)$$

$$u(t, 0) = u(t, 2\pi). \quad (22)$$

Previous studies have proved that it is hard for PINNs to resolve advection equation when the transport velocity  $\beta$  becomes larger. Here we set  $\beta$  as 100, which has never been tried by PINNs. To make it easier to resolve, the periodic boundary condition is directly imposed by a periodic layer [11]. EM-layer is adopted as the first hidden layer of Deeper-PINNs. More details of the hyper-parameter configuration can be found in Table 1.

Table 1: Advection equation: Hyper-parameter configuration.

Parameter	Value
<b>PirateNet</b>	
Layer size	100
Fourier feature scale	1.0
<b>Deeper-PINN</b>	
Sublayer size	100
Number of sublayers per EM-layer	2
<b>Training Parameters</b>	
Initial learning rate	0.001
Exponential decay steps	3,000
Decay rate	0.9
Training steps	120,000
Collocation points	5,000

The results and comparisons of PirateNets and Deeper-PINNs are shown in Figure 3. As can be seen in Figure 3 (a), the PirateNets fail to resolve this problem even with the layers increasing. For Deeper-PINNs, however, better results can be obtained with a deeper structure. Figure 3 (b) presents the training time of the 2 models. It can be observed that 45-layer Deeper-PINN takes the same amount of training time with 58-layer PirateNet but has about 50% more parameters. This indicates that Deeper-PINNs have better computational efficiency.

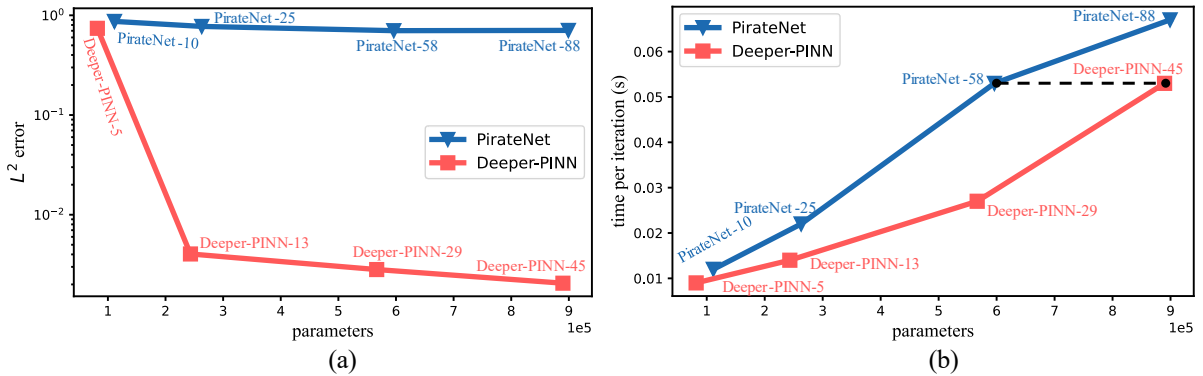


Figure 3: Advection equation: Comparison between Deeper-PINNs and PirateNets. (a)  $L^2$  error of PirateNet and Deeper-PINN in different depths. (b) Computing time of PirateNet and Deeper-PINN in different depths.

The loss and relative  $L^2$  test error during the training of the 2 models are shown in Figure 4. The training process of Deeper-PINN-29 shows 2 distinct stages, which are fitting stage and diffusion stage [28]. For the fitting stage, the model tries to escape from the local minimum local optimum [29]. After that, the model moves into the diffusion stage, where most of the learning occurs. Correspondingly, at around 20000 iterations, the fitting stage ends and the  $L^2$  test error decreases dramatically. However, for Deeper-PINN-5, PirateNet-10 and PirateNet-58, the training processes only show 1 stage, and the models fail to converge to correct solutions. This indicates that for Deeper-PINNs, a deeper structure enables the model to resolve complicated problems that a shallow structure cannot deal.

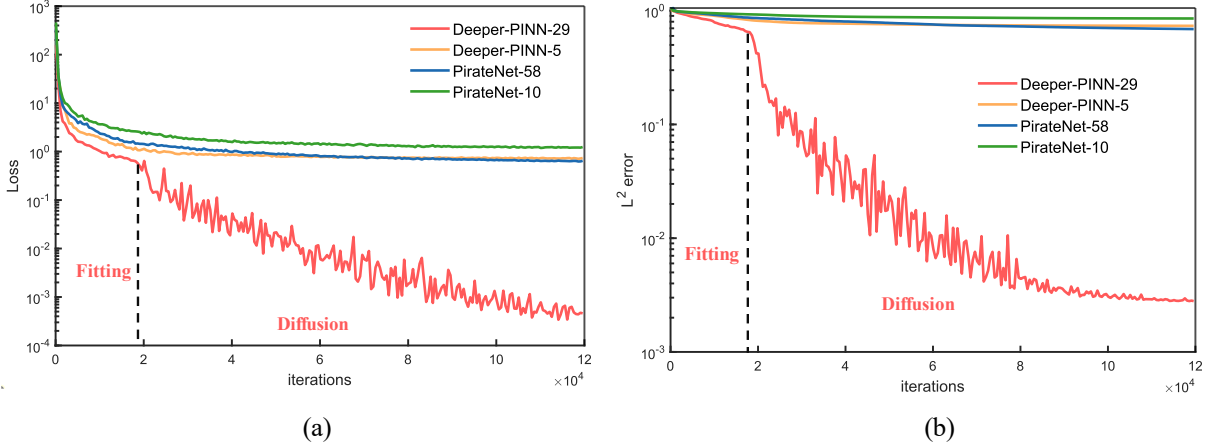


Figure 4: Advection equation: (a) Loss curve during the training processes. (b) Relative  $L^2$  test error during the training processes.

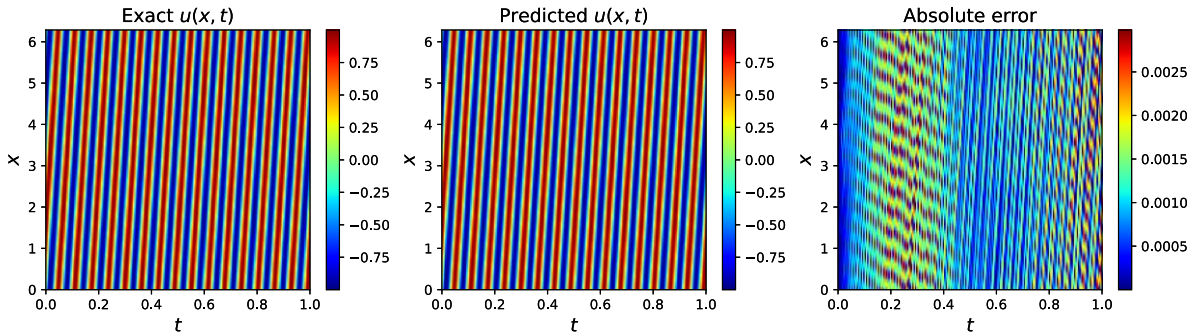


Figure 5. Advection equation: Comparison between prediction of Deeper-PINN and analytical solution. (a)  $L^2$  error of PirateNet and Deeper-PINN in different depths. (b) Computing time of PirateNet and Deeper-PINN in different depths.

The best result of 45-layer Deeper-PINN is shown in Figure 5. With  $L^2$  error of  $1.79e-3$ , the prediction shows good alignment with the exact solution.

## 1D Wave propagation

We study the 1D wave propagation problem expressed as below:

$$\frac{\partial^2 u}{\partial t^2} = c^2 \frac{\partial^2 u}{\partial x^2}, \quad (x, t) \in [0, 1] \times [0, 10], \quad (23)$$

$$u(0, t) = u(1, t) = 0, \quad t \in [0, T], \quad (24)$$

$$u(x, 0) = \sin(\pi x), \quad x \in [0, 1], \quad (25)$$

$$\frac{\partial u}{\partial t}(x,0)=0, \quad (26)$$

where we set  $c=1$ . The analytical solution for this problem is:

$$u(x,t)=\sin(\pi x)\cos(c\pi t). \quad (27)$$

Here the random Fourier features method is adopted as the first layer of Deeper-PINN. More details of the hyper-parameter configuration are listed in Table 2.

Table 2: 1D wave propagation: Hyper-parameter configuration.

Parameter	Value
<b>PirateNet</b>	
Layer size	100
Fourier feature scale	1.0
<b>Deeper-PINN</b>	
Sublayer size	100
Number of sublayers per EM-layer	3
Fourier feature scale	1.0
<b>Training Parameters</b>	
Initial learning rate	0.001
Exponential decay steps	500
Decay rate	0.9
Training steps	30,000
Collocation points	5,000

The comparisons of Deeper-PINNs and PirateNets are presented in Figure 6. Notice that for this problem, 2-layer Deeper-PINN achieves comparable  $L^2$  error of 124-layer PirateNet, with only about 5% parameters. The training time presented Figure 6 (b) indicates that PirateNets show better computational efficiency than PirateNets.

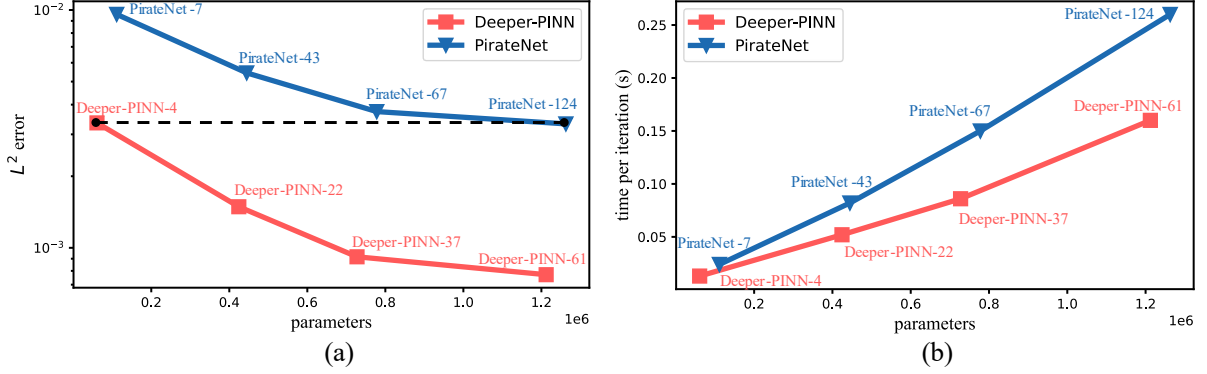


Figure 6. Wave propagation: Comparison between Deeper-PINNs and PirateNets. (a)  $L^2$  error of PirateNet and Deeper-PINN in different depths. (b) Computing time of PirateNet and Deeper-PINN in different depths.

The best result of 64-layer Deeper-PINN shows an  $L^2$  error of  $4.54e-4$ . The corresponding prediction is shown in Figure 7.

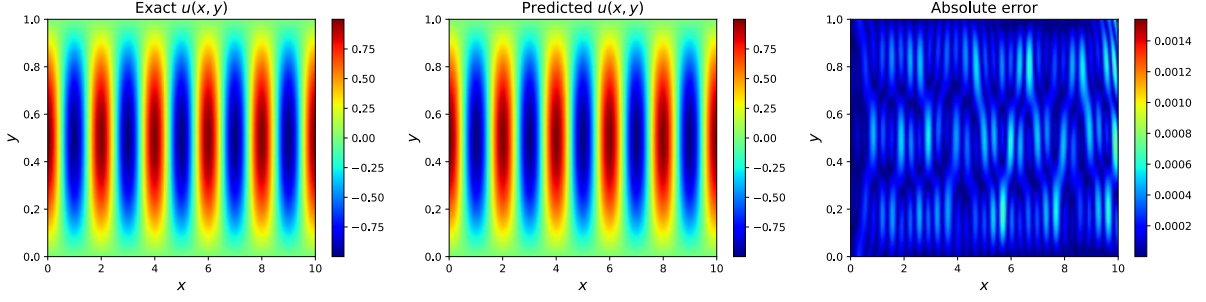


Figure 7. Wave propagation: Comparison between prediction of Deeper-PINN and analytical solution.

## Flow Mixing

We consider flow mixing problem, which is expressed as below:

$$\frac{\partial u}{\partial t} + a \frac{\partial u}{\partial x} + b \frac{\partial u}{\partial y} = 0, \quad (x, y, t) \in [-4, 4] \times [-4, 4] \times [0, 4] \quad (28)$$

$$a(x, y) = -\frac{v_t}{v_{t \max}} \frac{y}{r}, \quad (29)$$

$$b(x, y) = -\frac{v_t}{v_{t \max}} \frac{x}{r}, \quad (30)$$

$$v_t = \text{sech}^2(r) \tanh(r), \quad (31)$$

$$r = \sqrt{x^2 + y^2}, \quad (32)$$

The analytical solution is:

$$u(x, y, t) = -\tanh\left(\frac{y}{2} \cos(\omega t) - \frac{x}{2} \sin(\omega t)\right), \quad (33)$$

where  $\omega = \frac{1}{r} \frac{v_t}{v_{t \max}}$ .  $v_{t \max}$  is set as 0.385. The initial condition can be got from Equation.(33).

Random Fourier features method is utilized as the first hidden layer to enhance the expressive ability of Deeper-PINN. The details of the hyper-parameter configuration can be found in Table 3.

Table 3: Flow mixing: Hyper-parameter configuration.

Parameter	Value
<b>PirateNet</b>	
Layer size	128
Fourier feature scale	2.0
<b>Deeper-PINN</b>	
Sublayer size	128
Number of sublayers per EM-layer	2
Fourier feature scale	2.0
<b>Training Parameters</b>	
Initial learning rate	0.001
Training steps	50,000
Decay rate	0.9
Exponential decay steps	2,000
Collocation points	20,000

The results are presented in Figure 8. Although PirateNet shows better performance at shallow neural networks, Deeper-PINN obtains smaller  $L^2$  error when the neural networks become deeper. This indicates the superiority of Deeper-PINNs in deeper structures.



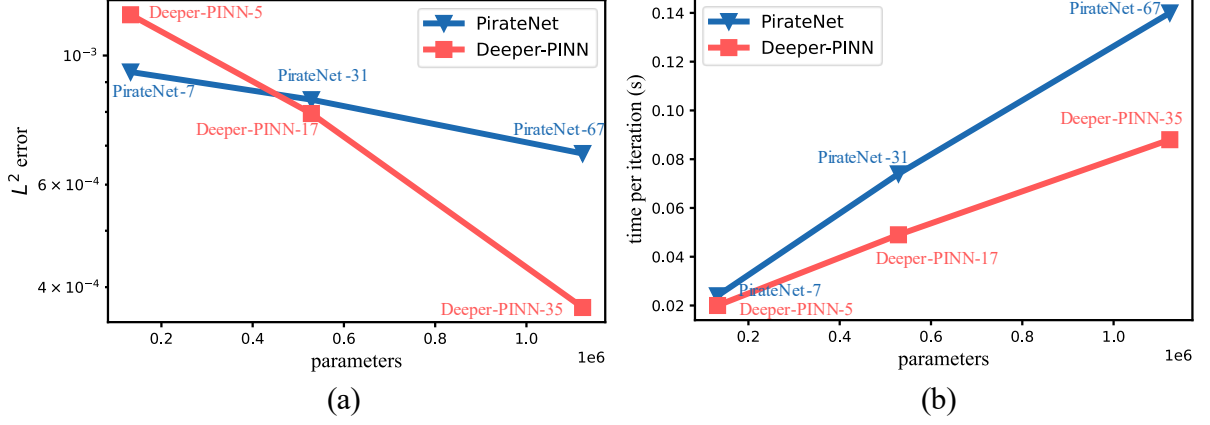


Figure 8. Flow mixing: Comparison of the PirateNets and Deeper-PINNs. (a)  $L^2$  error of PirateNet and Deeper-PINN in different depths. (b) Computing time of PirateNet and Deeper-PINN in different depths.

Figure 9 shows the predicted solution of PirateNet-35, with an  $L^2$  error of  $3.12e-4$ , the predicted solutions show good consistence with the exact solutions.

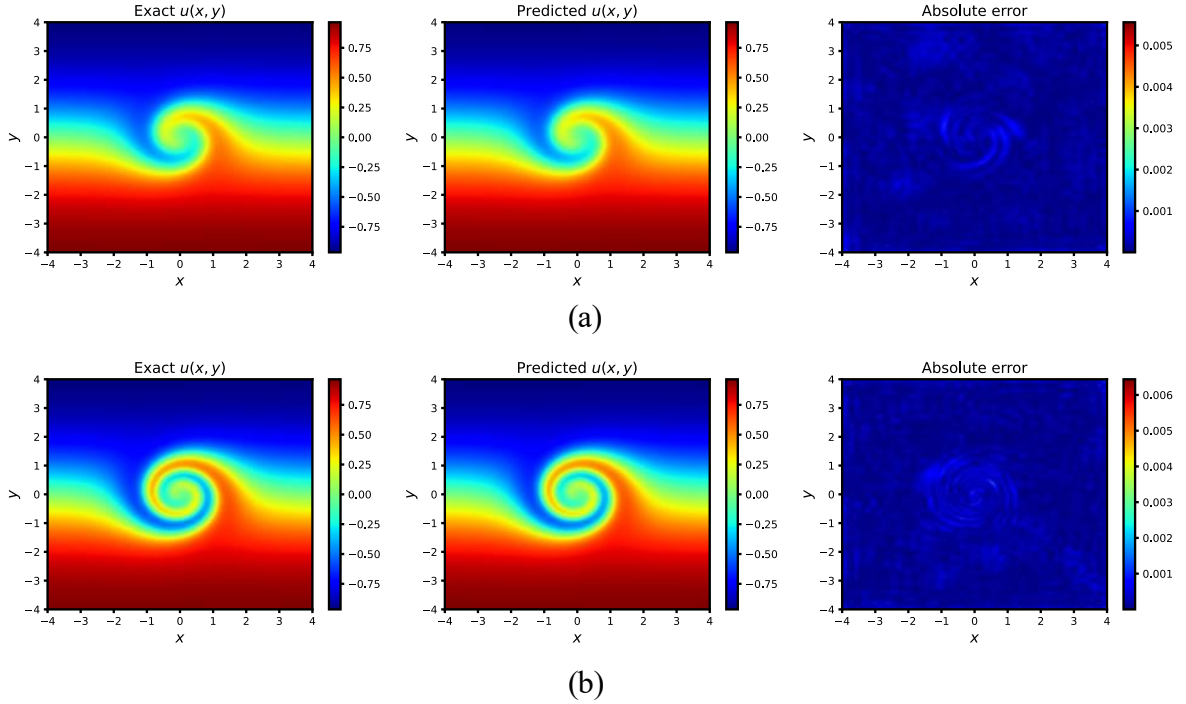


Figure 9. Flow mixing: Comparisons between prediction of Deeper-PINNs and analytical solutions (a)  $t = 2$ , (b)  $t = 4$ .

### Korteweg–De Vries equation

Korteweg–De Vries equation (KDV) expressed as below is considered.

$$u_t + \eta u u_x + \mu^2 u_{xxx} = 0, \quad t \in (0, 1), \quad x \in (-1, 1), \quad (34)$$

$$u(x, 0) = \cos(\pi x), \quad (35)$$

$$u(t, -1) = u(t, 1), \quad (36)$$

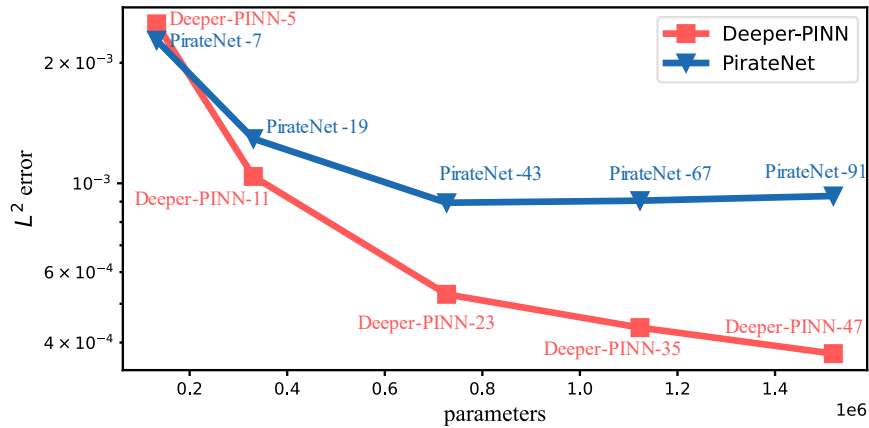
where we set  $\eta = 1$  and  $\mu = 0.022$ .

Table 4: KDV: Hyper-parameter configuration.

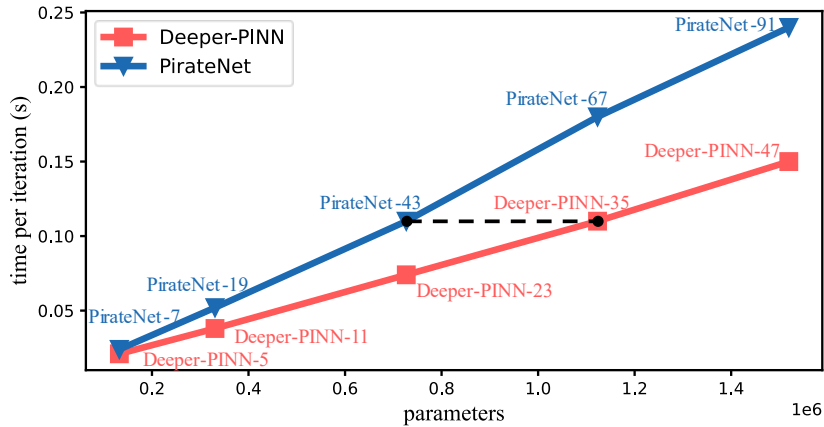
Parameter	Value
<b>PirateNet</b>	

Layer size	128
Fourier feature scale	2.0
<b>Deeper-PINN</b>	
Sublayer size	128
Number of sublayers per EM-layer	2
Fourier feature scale	2.0
<b>Training Parameters</b>	
Initial learning rate	0.001
Exponential decay steps	2,000
Decay rate	0.9
Training steps	120,000
Collocation points	5,000

The periodic boundary condition is directly imposed by a periodic layer. The random Fourier features method is adopted as the first hidden layer. More details of configuration can be found in Table 4.



(a)



(b)

Figure 10. KDV: Comparison of the PirateNets and Deeper-PINNs. (a)  $L^2$  error of PirateNet and Deeper-PINN in different depths. (b) Computing time of PirateNet and Deeper-PINN in different depths.

The results in Figure 10. reveal that Deeper-PINNs show better performance when the neural networks become deeper. And with the depth increasing, the differences become more and more distinct as PirateNets appear to be saturated with the layers increasing. Also note that with about the same training time, the 35-layer Deeper-PINN gets about 50% smaller  $L^2$  error than 43-layer PirateNet.

Figure 11 presents the best performance of 47-layer Deeper-PINNs, which shows good consistence with the exact solution. The  $L^2$  error is  $2.95e-4$ , which is the state-of-the-art of this case.

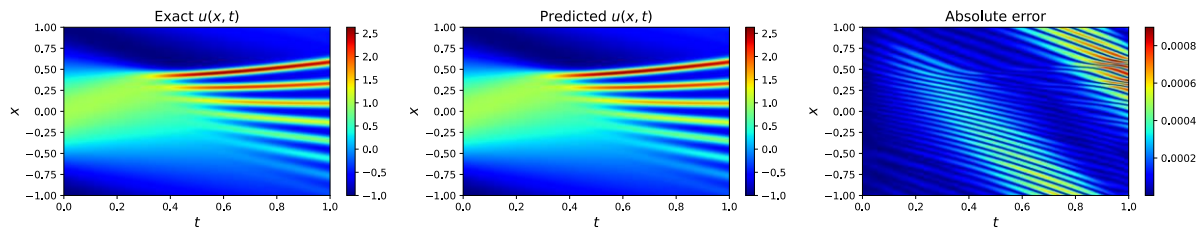


Figure 11. KDV: Comparison between prediction of Deeper-PINN and exact solution

## Conclusion

In this work, we proposed Deeper-PINNs, an element-wise multiplication based PINN structure. The element-wise multiplication operations could alleviate the initialization pathology of PINN and at the same time, improve the expressive ability of the neural network.

## References

- [1] M. Raissi, P. Perdikaris, and G. E. Karniadakis, "Physics-informed neural networks: A deep learning framework for solving forward and inverse problems involving nonlinear partial differential equations," *Journal of Computational physics*, vol. 378, pp. 686-707, 2019.
- [2] S. Cai, Z. Mao, Z. Wang, M. Yin, and G. E. Karniadakis, "Physics-informed neural networks (PINNs) for fluid mechanics: A review," *Acta Mechanica Sinica*, vol. 37, no. 12, pp. 1727-1738, 2021.
- [3] S. Cai, Z. Wang, S. Wang, P. Perdikaris, and G. E. Karniadakis, "Physics-informed neural networks for heat transfer problems," *Journal of Heat Transfer*, vol. 143, no. 6, p. 060801, 2021.
- [4] F. Jiang, M. Xia, and Y. Hu, "Physics-Informed Machine Learning for Accurate Prediction of Temperature and Melt Pool Dimension in Metal Additive Manufacturing," *3D Printing and Additive Manufacturing*, 2023.
- [5] G. S. Misyris, A. Venzke, and S. Chatzivasileiadis, "Physics-informed neural networks for power systems," in *2020 IEEE power & energy society general meeting (PESGM)*, 2020: IEEE, pp. 1-5.
- [6] S. Wang, X. Yu, and P. Perdikaris, "When and why PINNs fail to train: A neural tangent kernel perspective," *Journal of Computational Physics*, vol. 449, p. 110768, 2022.
- [7] S. Wang, H. Wang, and P. Perdikaris, "On the eigenvector bias of Fourier feature networks: From regression to solving multi-scale PDEs with physics-informed neural networks," *Computer Methods in Applied Mechanics and Engineering*, vol. 384, p. 113938, 2021.
- [8] S. Wang, Y. Teng, and P. Perdikaris, "Understanding and mitigating gradient flow pathologies in physics-informed neural networks," *SIAM Journal on Scientific Computing*, vol. 43, no. 5, pp. A3055-A3081, 2021.
- [9] R. Bischof and M. Kraus, "Multi-objective loss balancing for physics-informed deep learning," *arXiv preprint arXiv:2110.09813*, 2021.
- [10] N. Sukumar and A. Srivastava, "Exact imposition of boundary conditions with distance functions in physics-informed deep neural networks," *Computer Methods in Applied Mechanics and Engineering*, vol. 389, p. 114333, 2022.

- [11] S. Dong and N. Ni, "A method for representing periodic functions and enforcing exactly periodic boundary conditions with deep neural networks," *Journal of Computational Physics*, vol. 435, p. 110242, 2021.
- [12] S. Wang, S. Sankaran, and P. Perdikaris, "Respecting causality for training physics-informed neural networks," *Computer Methods in Applied Mechanics and Engineering*, vol. 421, p. 116813, 2024.
- [13] A. Krishnapriyan, A. Gholami, S. Zhe, R. Kirby, and M. W. Mahoney, "Characterizing possible failure modes in physics-informed neural networks," *Advances in Neural Information Processing Systems*, vol. 34, pp. 26548-26560, 2021.
- [14] J. Guo, Y. Yao, H. Wang, and T. Gu, "Pre-training strategy for solving evolution equations based on physics-informed neural networks," *Journal of Computational Physics*, vol. 489, p. 112258, 2023.
- [15] S. J. Anagnostopoulos, J. D. Toscano, N. Stergiopoulos, and G. E. Karniadakis, "Residual-based attention in physics-informed neural networks," *Computer Methods in Applied Mechanics and Engineering*, vol. 421, p. 116805, 2024.
- [16] L. D. McClenny and U. M. Braga-Neto, "Self-adaptive physics-informed neural networks," *Journal of Computational Physics*, vol. 474, p. 111722, 2023.
- [17] Y. Song, H. Wang, H. Yang, M. L. Taccari, and X. Chen, "Loss-attentional physics-informed neural networks," *Journal of Computational Physics*, vol. 501, p. 112781, 2024.
- [18] W. Li, C. Zhang, C. Wang, H. Guan, and D. Tao, "Revisiting PINNs: Generative adversarial physics-informed neural networks and point-weighting method," *arXiv preprint arXiv:2205.08754*, 2022.
- [19] A. Daw, J. Bu, S. Wang, P. Perdikaris, and A. Karpatne, "Mitigating propagation failures in physics-informed neural networks using retain-resample-release (r3) sampling," *arXiv preprint arXiv:2207.02338*, 2022.
- [20] M. A. Nabian, R. J. Gladstone, and H. Meidani, "Efficient training of physics-informed neural networks via importance sampling," *Computer-Aided Civil and Infrastructure Engineering*, vol. 36, no. 8, pp. 962-977, 2021.
- [21] F. Jiang, X. Hou, and M. Xia, "Densely Multiplied Physics Informed Neural Network," *arXiv preprint arXiv:2402.04390*, 2024.
- [22] J. Cho, S. Nam, H. Yang, S.-B. Yun, Y. Hong, and E. Park, "Separable physics-informed neural networks," *Advances in Neural Information Processing Systems*, vol. 36, 2024.
- [23] S. Wang, B. Li, Y. Chen, and P. Perdikaris, "PirateNets: Physics-informed Deep Learning with Residual Adaptive Networks," *arXiv preprint arXiv:2402.00326*, 2024.
- [24] A. Griewank and A. Walther, *Evaluating derivatives: principles and techniques of algorithmic differentiation*. SIAM, 2008.
- [25] N. Zobeiry and K. D. Humfeld, "A physics-informed machine learning approach for solving heat transfer equation in advanced manufacturing and engineering applications," *Engineering Applications of Artificial Intelligence*, vol. 101, p. 104232, 2021.
- [26] K. He, X. Zhang, S. Ren, and J. Sun, "Deep residual learning for image recognition," in *Proceedings of the IEEE conference on computer vision and pattern recognition*, 2016, pp. 770-778.
- [27] X. Glorot and Y. Bengio, "Understanding the difficulty of training deep feedforward neural networks," in *Proceedings of the thirteenth international conference on artificial intelligence and statistics*, 2010: JMLR Workshop and Conference Proceedings, pp. 249-256.

- [28] S. J. Anagnostopoulos, J. D. Toscano, N. Stergiopoulos, and G. E. Karniadakis, "Learning in PINNs: Phase transition, total diffusion, and generalization," *arXiv preprint arXiv:2403.18494*, 2024.
- [29] M. Zhou, T. Liu, Y. Li, D. Lin, E. Zhou, and T. Zhao, "Toward understanding the importance of noise in training neural networks," in *International Conference on Machine Learning*, 2019: PMLR, pp. 7594-7602.